Surface & Coatings Technology 420 (2021) 127327

Contents lists available at ScienceDirect

Surface & Coatings Technology

journal homepage: www.elsevier.com/locate/surfcoat

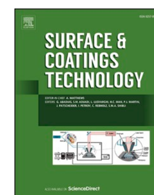

Phase formation and mechanical properties of reactively and non-reactively sputtered Ti-B-N hard coatings

R. Hahn [a,b,*], A. Tymoszuk [a], T. Wojcik [a], A. Kirnbauer [b], T. Kozák [c], J. Čapek [c], M. Sauer [d], A. Foelske [d], O. Hunold [e], P. Polcik [f], P.H. Mayrhofer [b], H. Riedl [a,b]

[a] Christian Doppler Laboratory for Surface Engineering of high-performance Components, TU Wien, A-1060 Wien, Austria
[b] Institute of Materials Science and Technology, TU Wien, A-1060 Wien, Austria
[c] Department of Physics and NTIS - European Centre of Excellence, University of West Bohemia, Plzen, Czech Republic
[d] Analytical Instrumentation Center, TU Wien, A-1060 Wien, Austria
[e] Oerlikon Balzers, Oerlikon Surface Solutions AG, FL-9496 Balzers, Liechtenstein
[f] Plansee Composite Materials GmbH, D-86983 Lechbruck am See, Germany

ARTICLE INFO

Keywords:
Physical vapor deposition
Non-reactive magnetron sputtering
Fracture toughness
Ti-B-N

ABSTRACT

In the field of hard protective coatings, nano-crystalline Ti-B-N films are of great importance due to the adjustable microstructure and mechanical properties through their B content. Here, we systematically study this influence of B on Ti-B-N during reactive as well as non-reactive DC magnetron sputtering. The different deposition routes allow for an additional, very effective key parameter to modify bond characteristics and microstructure. Plasma analysis by mass spectroscopy reveals that for comparable amounts of Ti^+, Ti^{2+}, Ar^+, and Ar^{2+} ions, the count of N^+ ions is about 2 orders of magnitude lower during non-reactive sputtering. But for the latter, the N^+/N_2^+ ratio is close to 1, whereas during reactive sputtering this ratio is only 0.1. This may explain why during reactive deposition of Ti-B-N, the B—N bonds dominate (as suggested by X-ray photoelectron spectroscopy), whereas the B—B and Ti—B bonds dominate for non-reactively prepared Ti-B-N. Chemically, reactively versus non-reactively sputtered Ti-B-N coatings follow the TiN-BN versus TiN-TiB_2 tie line, respectively. Detailed X-ray diffraction and transmission electron microscopy studies reveal, that up to 10 at.% B can be dissolved in the fcc-TiN lattice when prepared by non-reactive sputtering, whereas already for a B content of 4 at.% a BN-rich boundary phase forms when reactively sputtered. Thus, we could not only observe a higher hardness (35 GPa instead of 25 GPa) as well as a higher indentation modulus (480 GPa instead of 260 GPa), but also a higher fracture energy (0.016 instead of 0.009 J/m during cube-corner indentations) for Ti-B-N coatings with 10 at.% B, when prepared non-reactively.

1. Introduction

Physical vapor deposited (PVD) TiN is an extremely successful coating, not just for decorative purposes (due to its shiny yellow color) or diffusion barrier abilities (e.g., for microelectronics), but also to protect cutting tools against heavy mechanical and corrosive loads, since the 1960s [1]. To even further increase the efficiency of such products, technological innovations for the preparation of higher quality coatings have been made [1–3] but also their microstructure [4,5] and/or chemistry have been modified. A massive increase in performance, even a breakthrough, came with chemically modifying the metal sublattice (developing $Ti_{1-x}Al_xN$ [6,7]) or the non-metal sublattice (TiC_xN_{1-x} [8,9]). Boron is a special alloying element (due to its semi-metallic character), as it may occupy the metal [10] as well as non-metal sublattice [10,11] and easily forms BN-rich boundary phases [12]. This leads to many diverse studies, reporting about a significant hardness increase of TiN with the addition of B (up to 40 GPa) [13–19], but also about a hardness decrease [20,21].

When plotting the chemical composition of individual Ti-B-N coatings in the corresponding equilateral concentration triangle, hard and superhard (> 40 GPa [22]) coatings are centered along the TiN-TiB_2 or TiN-TiB tie lines [10,13–17,23–26]. The softer ones are along the TiN-BN or TiB_2-BN tie lines, deeper within the TiN-BN-TiB_2 triangle, or closer to the BN region [21,27,28]. As boron is slightly larger than

* Corresponding author at: Institute of Materials Science and Technology, TU Wien, Getreidemarkt 9/E308, A-1060 Vienna, Austria.
E-mail address: rainer.hahn@tuwien.ac.at (R. Hahn).

https://doi.org/10.1016/j.surfcoat.2021.127327
Received 2 March 2021; Received in revised form 27 April 2021; Accepted 16 May 2021
Available online 24 May 2021
0257-8972/© 2021 The Authors. Published by Elsevier B.V. This is an open access article under the CC BY license (http://creativecommons.org/licenses/by/4.0/).

Table 1
Summarized deposition parameter for reactively and non-reactively magnetron sputtered Ti-B-N coatings.

	Target current (A)					Negative bias potential (V)	T_{sub} (°C)	Gas flow (sccm)		p_{dep} (Pa)
	2″ Ti	3″ TiN	2″ TiB_2	3″ TiB_2	3″ TiBN			Ar	N_2	
Reactive	0.6	–	–	0.05–0.6	–	60	480	7	3	0.4
Non reactive (binaries)	–	0.75	0.0–0.6	–	–	60	480	10	–	0.4
Non reactive (ternaries)	–	–	–	–	0.75	60	480	10	–	0.4

nitrogen (0.85 and 0.65 Å for the atomic radii of B and N, and 0.84 and 0.71 Å for the covalent bonding radii of B and N, respectively [29,30]), it leads to severe lattice distortions and larger lattice parameters when substituting for N in the TiN lattice [10,26]. The additionally changed bond characteristic leads to a dielastic contribution in the solid solution strengthening mechanisms. If the supply of B is too high to be completely dissolved in the crystal lattice, B-segregation will hinder coalescence during nucleation of the films as well as inhibit coarsening during growth of the film, leading to small-grained structures allowing for grain-boundary strengthening (often described by the Hall-Petch relation [31,32]). A similar effect is obtained when two competing and essentially immiscible phases (such as TiN and TiB_2) nucleate and grow simultaneously [25]. A decrease in hardness (upon adding B to TiN) is often related to the formation of weaker B—N bonds, typically present in pronounced amorphous grain boundary phases of the coating microstructures [21]. But these B—N dominated grain boundary phases are able to reduce the coefficient of friction [20]. Such phase formation is often observed as a result of reactive deposition processes, whereas non-reactive deposition routes typically lead to superior hardnesses [13,21]. Consequently, not just the B-content defines the phase formation and resulting properties but also the deposition routes. Besides the beneficial properties of high hardness or low friction coefficient, a major drawback of Ti—N as well as Ti-B-N coatings is their limited capability for plastic deformation, they are rather brittle. This restricts their application and often leads to premature failure in use. Recent studies [33,34] in the field of non-reactively sputtered transition metal carbonitrides highlighted an enhancement of fracture characteristics through a non-reactively deposition route.

Here, we analyze in detail the microstructure, phase formation, and mechanical properties (including consumed fracture energy during cube corner indentation) of reactively and non-reactively sputtered Ti-B-N coatings. Plasma analysis by mass spectroscopy allows linking these characteristics with the prevailing plasma composition. Non-reactive depositions were realized through co-sputtering of ceramic TiN and TiB_2 targets, as well as a $(TiN)_{0.5}(TiB_2)_{0.5}$ compound target (to realize higher boron content compared to co-sputtering) in an Ar glow discharge. Reactive depositions are realized through co-sputtering of a Ti and a ceramic TiB_2 target in a mixed Ar + N_2 glow discharge.

2. Experimental

All coatings were developed using an AJA International Orion 5 sputter deposition system equipped with two 2″ and one 3″ unbalanced magnetron sources. These and the applied bias potential were powered by two ENI RPG 50 (MKS Instruments) and two DCXS-4 (Sairem) DC power supplies. Argon was introduced at the bottom of the chamber; the nitrogen inlet is placed near the heated and rotating substrate holder (1 s^{-1}). The substrates (sapphire $(1\bar{1}02)$ and silicon (100)) were cleaned in acetone and ethanol (5 min each) in an ultrasonic bath, subsequently placed via a load lock in the chamber. Furthermore, the substrates were thermally cleaned at the deposition temperature for 20 min (600 °C heater temperature, equivalent to 480 °C substrate surface temperature), and subsequently, Ar plasma etched for 10 min (by applying a negative bias potential of −750 V at an Argon pressure of 6 Pa). During the last 3 min of this substrate etching step, all targets were cleaned from possible surface contaminations by igniting their glow discharges as well. Half a minute before opening the shutters in front of the targets and thus starting the deposition, we reduced the total pressure to the actual deposition pressure (0.4 Pa) and added nitrogen. The latter is only needed for the reactive depositions and to obtain the desired poisoning state (steady-state region) of the Ti target, when the deposition starts. Reactively prepared coatings are co-sputtered from two 2″ Ti Targets and one 3″ TiB_2 target. The non-reactively prepared coatings were realized by co-sputtering of one 3″ TiN target and one 2″ TiB_2 target. An additional non-reactively sputtered coating was developed with one 3″ TiN-TiB_2 compound target (50 mol% TiN and 50 mol% TiB_2, i.e. $(TiN)_{0.5}(TiB_2)_{0.5}$ or $Ti_{0.4}B_{0.4}N_{0.2}$). The change in target dimensions, as well as the usage of a compound target, was necessary to obtain coatings with higher boron contents. All of the used targets had a purity of 99.5% and were produced by Plansee Composite Materials GmbH. The target-substrate distance was 110 mm, and the cathodes are con-focally arranged. The total gas flow was 10 sccm for all depositions, 3 sccm N_2 + 7 sccm Ar for the reactive ones, whereas all non-reactive coatings were deposited at 10 sccm Ar. The total pressure was controlled through a pressure controller to 0.4 Pa. Furthermore, we applied a bias potential of −60 V DC to the substrates to achieve a dense coating microstructure [35]. All targets were operated in current-controlled mode. We applied 0.6 A to both 2″ Ti targets and varied the current between 0.05 and 0.6 A on the 3″ TiB_2 target to deposit a variation in boron content for the reactively sputtered coatings. The 3″ TiN of the non-reactively deposited thin films was powered with a constant current of 0.75 A, the powering of the 2″ TiB_2 target was varied between 0 and 0.6 A, and the $(TiN)_{0.5}(TiB_2)_{0.5}$ composite target was operated with 0.75 A. The deposition parameters are summarized in Table 1.

Mass spectroscopy measurements during reactive or non-reactive magnetron sputtering of Ti—N were conducted in a slightly smaller vacuum chamber (506 mm in diameter and 522 mm in height) and pumped by a diffusion pump. This system is equipped with a 4″ magnetron (VTech, Gencoa Ltd) allowing for in-situ control of the magnetic field strengths over the Ti or the TiN targets (99.99% purity, 6 mm thick, Plansee Composite Materials GmbH). The magnetic field strength was adjusted to meet the waveforms of the target voltage and the target current density observed during the depositions of the films in the AJA International Orion 5 system.

The base pressure before starting each experiment was below than $2{\cdot}10^{-3}$ Pa. Argon was introduced into the chamber at a flow rate of 17 sccm and the pressure was set to 0.4 Pa. The magnetron was driven by a high-power pulsed direct current power supply (SIPP2000USB, Melec GmbH). The discharge was operated in DC mode either at a constant average discharge power of 600 W and varying Nitrogen content (for the reactive deposition) or with varying discharge power in pure Argon. The ions in the discharge plasma were analyzed by an energy-resolved mass spectrometer (Hiden Analytical EQP300) whose sampling orifice was directly facing the center of the target and the target–orifice distance was 150 mm. The extractor voltage was set to −3 V with respect to ground potential and the electrode controlling the ion energy was scanned from −5 to +55 V, which ensured that the whole ion energy distribution function was recorded. The dwell time for ion detection at

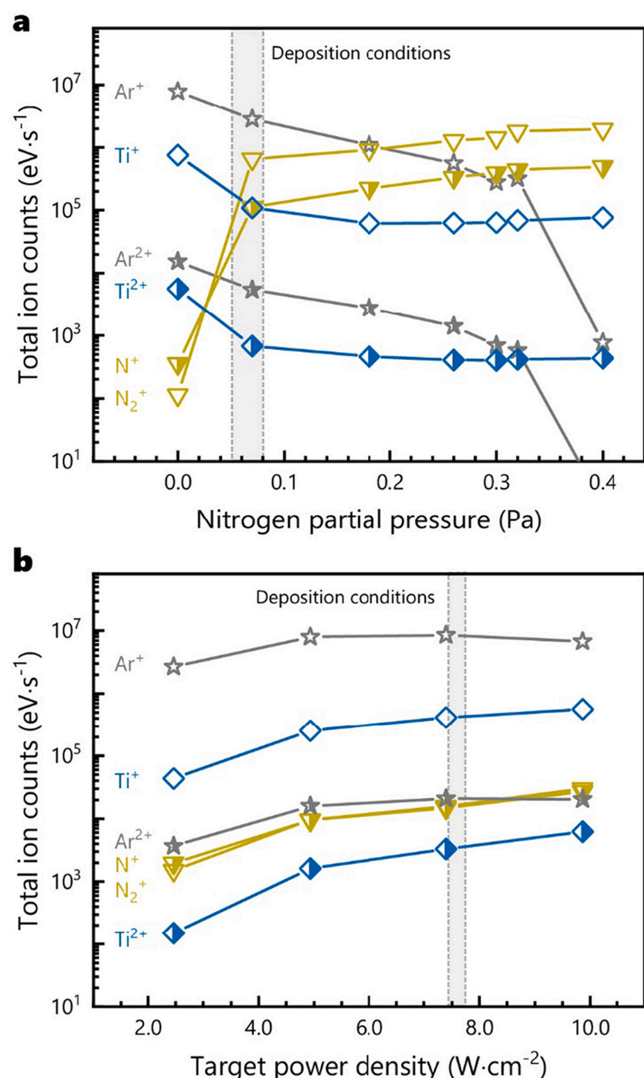

Fig. 1. Total ion counts of Ar^+, Ar^{2+}, Ti^+, Ti^{2+}, N_2^+, and N^+ measured at substrate position during magnetron sputtering. 2a shows the data for reactive sputtering with respect to the Nitrogen partial pressure. 2b shows the respective ion counts for non-reactive (pure Ar atmosphere) sputtering of a TiN target as a function of the varied target power density. The total pressure was set to 0.4 Pa in all experiments.

each energy was 100 ms. The mass spectrometer was tuned to $^{40}Ar^+$ ions and the obtained setting was kept constant for all measurements. Standard time-averaged acquisitions of ion energy spectra were measured for $^{40}Ar^+$, $^{40}Ar^{2+}$, $^{48}Ti^+$, $^{48}Ti^{2+}$, $^{14}N_2^+$ and $^{14}N^+$ ions. For each species, the total ion count was obtained by integrating the ion energy distribution function over the whole energy range.

X-ray photoelectron spectroscopy (XPS) of all Ti-B-N coatings was conducted with a custom-built SPECS XPS-spectrometer equipped with a monochromatic Al-K_α X-ray source (μFocus 350, spot size: 450 μm, power: 70 W) and a hemispherical WAL-150 analyzer (Acceptance angle 60°). Prior to XPS measurements the sample was sputter cleaned for 30 s on a 2 × 2 mm^2 area using 3 kV Ar-ions (angle between Ar beam and sample surface normal: 45°).

The overview and detailed spectra were recorded with pass-energies of 100 eV and 30 eV, and energy resolutions of 1.0 eV and 0.1 eV, respectively. These were analyzed using transmission corrections (as per manufacturer's specifications), Shirley-backgrounds, and sensitivity parameters after Scofield [36] within CASA XPS, and charge corrections (by setting the binding energy value of adventitious carbon from minor surface contamination to 284.8 eV, according to ISO 15472:2010). Deconvolution of XPS signals was carried out using symmetric Gaussian-Lorentzian peaks (GL(30)) and Levenberg-Marquardt least-square peak fitting.

X-ray diffraction patterns, recorded for all Ti-B-N coatings using a Panalytical XPert II θ-θ diffractometer equipped with a Cu-K_α source (λ = 0.15418 nm) in Bragg-Brentano geometry, were evaluated for peak positions as well as the full width at half maximum (FWHM) by using the commercial HighScore Plus software from Panalytical. In a first step we determined the background, manually defined peak positions, and subsequently fitted the Pearson VII function by a built-in algorithm based on a least-squares method.

Detailed investigations of the nanostructure and phase constitution are conducted via transmission electron microscopy (TEM, FEI TECNAI F20) combined with selected area electron diffraction (SAED). The images were recorded in bright field (BF) as well as in dark field (DF) mode (on the 111 and 200 rings of the fcc lattice) to enhance the visibility of single grains. Furthermore, Fast Fourier Transformation (FFT) and inverse FFT images were calculated using Gatan Digital Micrograph 3.

Indentation hardness, H, and indentation modulus, E, of our coatings were measured using a UMIS nanoindentation system equipped with a diamond Berkovich tip. We applied guidelines given by Oliver and Pharr [37] and Mencik et al. [38] to evaluate the obtained load-displacement curves. The applied maximum load varied between 3 and 45 mN and we performed a total number of 31 indentations per sample. The cube-corner indentations were performed using the same nanoindenter applying forces between 100 and 350 mN. We analyzed the resulting cube corner indents in an FEI Quanta 250 FEGSEM and evaluated the required energy for fracture by calculating the area of a pop-in event during indentation using Wolfram Mathematica 12 [39].

Biaxial residual stresses of as deposited coatings, including thermal stresses, are analyzed with the Stoney equation from the curvature of coated Si substrates, as obtained by optical profilometry (Nanovea PS 50). The initial curvature of the substrates was assumed to be zero.

3. Results and discussion

3.1. Deposition: plasma- and elemental composition

To understand the differences between reactive and non-reactive sputtered nitrides, we investigated the sputtering atmosphere by mass spectroscopy (Fig. 1) in a separate chamber for pure TiN. Although with this technique only the ion fluxes can be evaluated (there is no direct information about neutrals), they provide important information on the discharge conditions. Fig. 1a shows the total ion count for various nitrogen partial pressures during reactive sputtering, whereas the nitrogen partial pressure used for the preparation of our films is indicated by the grey bar. For the non-reactive case, we varied the target power density, see Fig. 1b (the power density used for the preparation of our films is labeled by the grey shaded area). Although the titanium ion counts (Ti^+ and Ti^{2+} see open and half-filled diamond symbols) are comparable for the deposition conditions used, the titanium to nitrogen (N^+ and N_2^+ see half-filled and open triangles) ion ratio is about 13.7 for the non-reactive discharge, and only 0.14 for the reactive case. In addition, the fraction $N^+/(N^+ + N_2^+)$ is 51% during non-reactive discharges and only 15% during reactive discharges. Thus, there is especially an oversupply of the less-reactive N_2^+ ions with respect to titanium ions during reactive sputtering in addition to the obvious oversupply of neutral N_2 as well. Still no N_2 gas is introduced during non-reactive sputtering, there is still a significant amount of N_2^+ in the discharge with about 49% of the nitrogen ions, see Fig. 1b. In comparison, during reactive sputtering the N_2^+ ions are about 85% of all nitrogen ions. This may in part explain the significant difference in deposition rate, which is about 3-times lower for the reactive case (6.9 nm·min^{-1} in the reactive case with two 2″ Ti targets compared to 23.4 nm·min^{-1} in the non-reactive case with one 3″ TiN target), where the growing film is terminated with less-reactive N_2^+

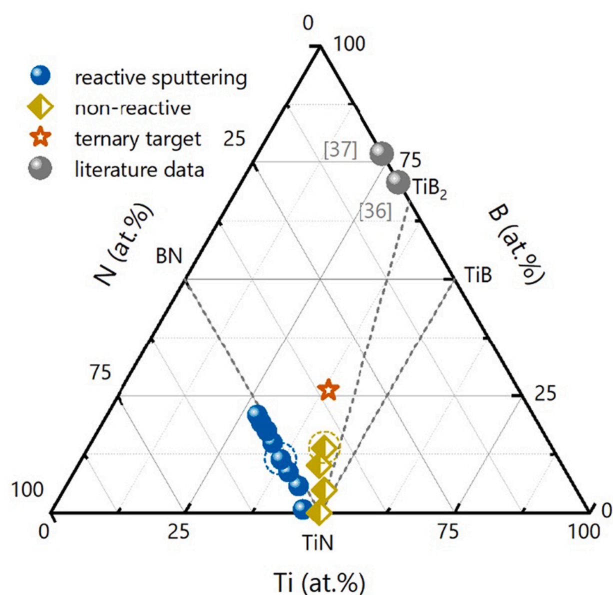

Fig. 2. Isothermal section of the ternary Ti-B-N system with the chemical compositions of all coatings deposited. The data points were measured using XPS, the TiN-TiB_2, TiN-TiB, and TiN-BN tie lines are plotted as dashed lines. To present a ternary diagram, the elemental compositions were recalculated to meet the condition Ti + B + N = 100 at.%. Further mentions of the boron content refer to the measured B content. The circled samples are investigated in detail later in the manuscript.

or even N_2. The thicknesses of the reactive coatings with increasing B content were the following: 0.718, 0.705, 0.809, 0.951, 1.23, 1.67, 2.05, and 2.19 μm. For our non-reactive depositions, we observed 2.11, 2.12, 2.16, 2.13, and 1.82 μm with increasing B content. But this not just has implications on the deposition rate, also the phase formation (being always dependent on energy and kinetic) may be influenced. For TiN, as long as there is sufficient N supply, the phase is still TiN with a likely over stoichiometric composition of N/Ti >1. But for other materials such as Ti-B-N, this can also modify the dominating bond character from Ti—B or TiN towards B—N.

To estimate the flux of species arriving at the substrate (for the reactive as well as non-reactive sputter deposition of TiN) we used the following assumptions and formulae. For the sputtered Ti species, we calculated the sputtering rate of Ti using the known target current and the sputtering yield of Ti. Then we used the SIMTRA software [40] to calculate the fraction of sputtered atoms arriving at the substrate. The SIMTRA software calculates the transport of individual sputtered atoms in a homogeneous background gas using a Monte Carlo method. The simulation parameters and geometry corresponded to the experimental system used. Based on this, an arrival flux of two times 4.4×10^{15} $cm^{-2} \cdot s^{-1}$ Ti species during reactively sputtering the two 2″ Ti targets was estimated (10^{16} Ti species per second and cm^2). For the reactive gas, we measured the N_2 partial pressure as follows: we started the deposition process at the desired flow rate ratio and the total pressure of Ar and N_2, then we switched off the N_2 flow (at fixed throttle valve position) and determined the complement to the total pressure as the N_2 partial pressure. This yielded a value of 0.08 Pa. From this partial pressure and assuming the thermal velocity of the gas, we calculated the flux of Nitrogen onto the substrate as:

$$\dot{\Gamma} = \frac{p}{\sqrt{2 \cdot \pi \cdot m \cdot k \cdot T}}$$

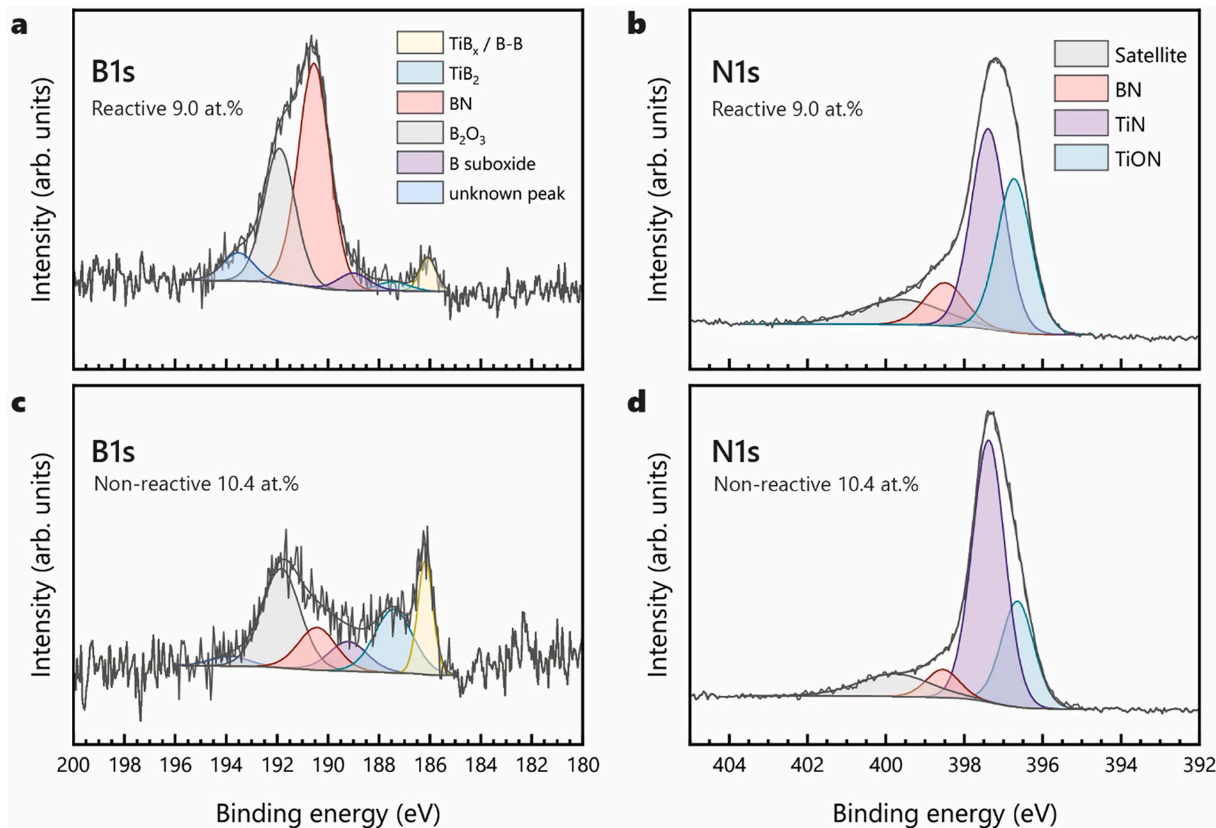

Fig. 3. XPS detail spectra of the B1s region of 3a: the reactively deposited coating, 3c: the non-reactively deposited coating, as well as the detail spectra of the N1s region of the reactively and non-reactively deposited coating (3b and 3d respectively).

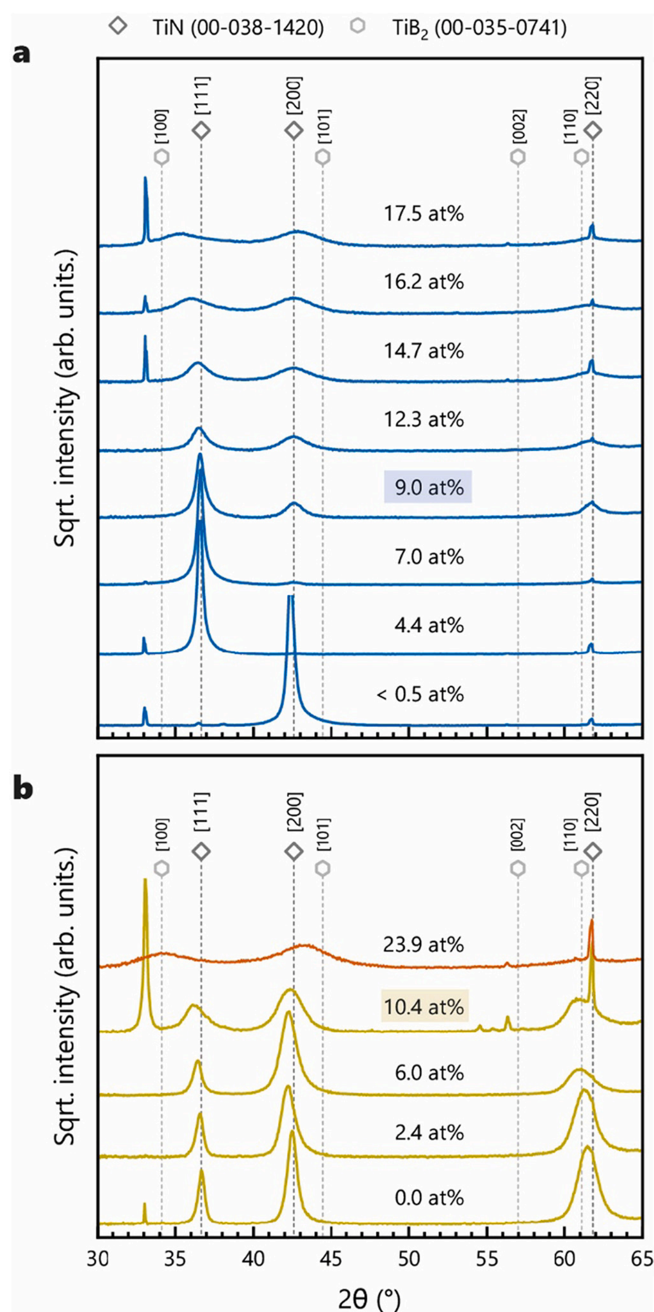

Fig. 4. X-ray diffraction patterns (Bragg-Brentano) of our Ti-B-N coatings. 4a shows the XRD patterns of the reactively deposited coatings, 4b the XRD pattern of the non-reactively deposited coatings. The patterns are labeled with the Boron content of the thin film.

where p is the partial pressure, m is the mass of the gas atom or molecule, k the Boltzmann constant, and T the gas temperature. Using a temperature range between 350 K and 650 K (substrate temperature) and a partial pressure of 0.08 Pa, we obtained a flux between 1.51×10^{17} and $2.05 \times \cdot 10^{17}$ $cm^{-2} \cdot s^{-1}$ N_2 species, hence in the order of 10^{17}. This would leave us with at least one order of magnitude oversupply of N with respect to Ti. This oversupply, however, is not present during non-reactive sputtering as the working gas within the chamber is just Ar. Thus, the resulting ratio of film-forming species (Ti and N) is following the target composition, except for different sputter angle distributions and gas scattering events. Calculating the arriving fluxes with SIMTRA yields 4.4×10^{15} $Ti/cm^{-2} \cdot s^{-1}$ for the non-reactive case, being essentially the same as the nitrogen flux during non-reactive sputtering with 4.2×10^{15} $N/cm^{-2} \cdot s^{-1}$ (assuming a sputter yield of 0.4 for Ti and N from TiN [41]). Thus, especially the arrival flux of N species is significantly lower during non-reactive sputtering and better matches that of Ti than during reactive sputtering. This partly explains the significantly lower deposition rates during reactive sputtering, as the growing film surface is decorated with adsorbed N_2.

XPS measurements reveal a fundamental difference in elemental compositions depending on the type of process used depositing the different Ti-B-N coatings. While non-reactive co-sputtering of TiN and TiB_2 targets, as well as non-reactive sputtering of the $(TiN)_{0.5}(TiB_2)_{0.5}$ target results in coatings with compositions near the TiN-TiB_2 tie line, the reactive co-sputtering of Ti and TiB_2 targets, leads to composition along the TiN-BN tie line – see Fig. 2. The non-reactively sputtered coatings are slightly over stoichiometric, especially with respect to the B content. The stoichiometry of TiB_2 coatings, when prepared from stoichiometric TiB_2 targets, strongly depends on various deposition conditions such as the Ar pressure (with increasing Ar pressure the B/Ti at.%-ratio decreases, even below 2 [42]), the target-to-substrate distance (with increasing distance the B/Ti at.%-ratio decreases below 2 [42]), as well as the Ar^+/Ti flux ratio (with increasing Ar^+/Ti ratio the B/Ti at.%-ratio increases, even above 3 [43,44]).

Therefore, we investigated in the detail the boron B1s and nitrogen N1s regions of Ti-B-N films prepared by reactive and non-reactive sputtering (Fig. 3).

By trend, the B 1s spectra for the reactively sputtered films are dominated by boron species in the higher binding energy range (> 190.5 eV), whereas films prepared from the non-reactive process show pronounced intensities in the lower binding energy range of the B 1s region (< 188 eV) which is exemplarily shown for two films having a comparable B content of 9.0 at.% for the reactively prepared one (Fig. 3a) and 10.4 at.% for the non-reactively prepared one (Fig. 3c). Additionally, those two coatings show similar XRD patterns and reveal the largest differences in the mechanical properties (both shown later in this work). Deconvolution of B 1s spectra suggests six different boron species: substoichiometric TiB_x overlapping with the signal of B—B at 186.2 eV, TiB_2 at 187.5 eV, Boron suboxides at 189.1 eV, B—N at 190.4 eV, B_2O_3 at 191.9 eV (see [45–49] and references therein) as well as an additional signal around 193.5–194.0 eV, which might be assigned to boric acid [50] but its exact nature remains elusive. There are significant differences between the relative intensities of boron species for the investigated samples. The difference in the B—N bond proportion may also be observed in the N1s signals (Fig. 3b and d for reactive and non-reactive sputtering, respectively), where we evidence an increased amount in the reactive case. Deconvolution of the N1s signals shows B—N bonds at 398.5 eV [46,47], TiN at 397.4 eV, and TiON at 396.7 eV as well as another component at 399.7 eV that has also been observed for TiN/TiON [51].

Based on this, a formation of B—N rich grain boundary phases is assumed during reactive depositions.

3.2. Structure and morphology

However, XRD studies do not show any formation of a crystalline BN phase in our reactively sputtered films (see Fig. 4a), but indicate that with increasing B content the intensity of the TiN-based XRD peaks reduces significantly while increasing the width. This is a strong indication for a massive reduction in coherently diffracting domain sizes with increasing B content (especially, with B $\geq$ 12.3 at.%), hence increasing B—N bonds for the reactively prepared films. The coating with the lowest B content (0.5 at.%) grows with a strongly preferred 002-orientation, which immediately shifts to a strongly preferred 111-orientation for higher B contents up to B $\leq$ 9.0 at.%. The coatings with 4.4 $\leq$ B $\leq$ 9.0 at.% have a lattice parameter of 4.25 $\pm$ 0.001 Å, while that for the coating with only 0.5 at.% B is slightly larger with 4.26 $\pm$ 0.001 Å. From 12.4 at.% B onwards, the growth orientation is more random and there is also a significant shift in position of the XRD peaks. But interestingly the

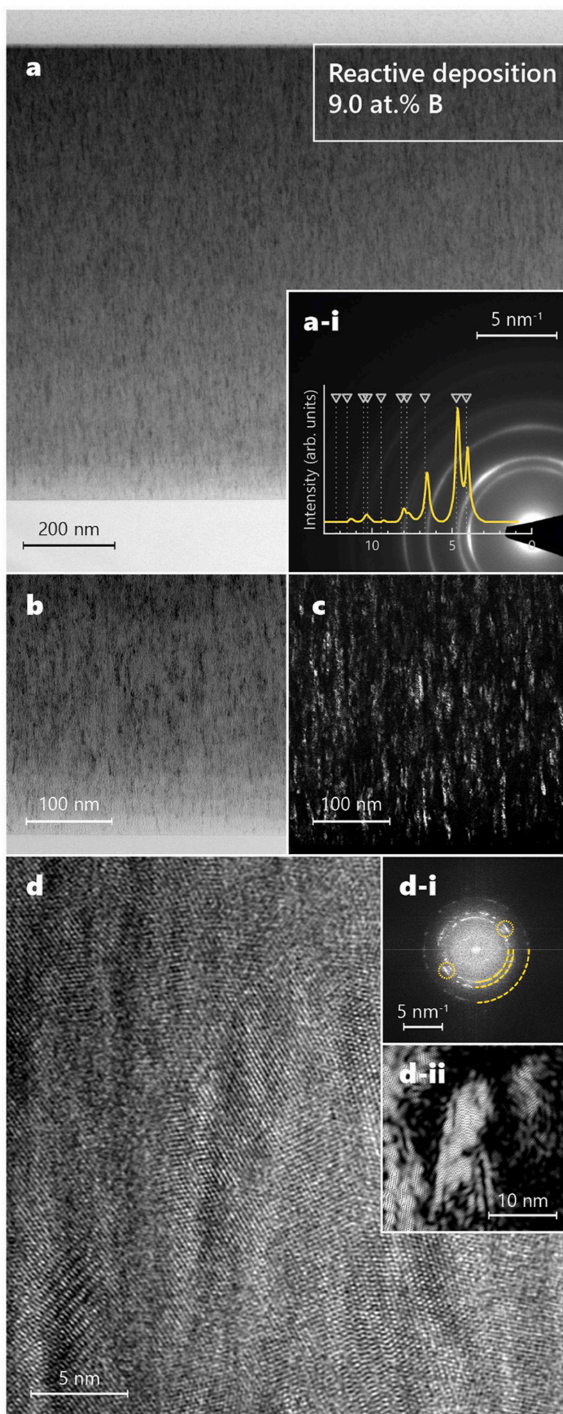

Fig. 5. TEM micrographs of the reactively deposited hard coating with 9.0 at.% B. 5a shows a bright field overview image of the coating, the substrate is on the bottom section of the micrograph. The inset a-I shows a representative selected area electron diffraction pattern of this coating, including an intensity integration, using CrystBox [56,57], of this pattern as an overlay. The triangle positions in this overlay mark the positions of a c-TiN reference (00-038-1420). 5b shows a higher magnification of this coating and 4c a dark field image (111 and 200 reflections are included) of the same area. 5d shows a high-resolution image of the coating. The inset d-i shows an FFT image of the whole area, the quarter rings mark the (111), (200), and (220) reflection of the TiN reference (00-038-1420), the inset d-ii shows an inverse FFT, where the marked areas in d-i (dotted rings around (111) and (200) rings) were used to recalculate the HR-image.

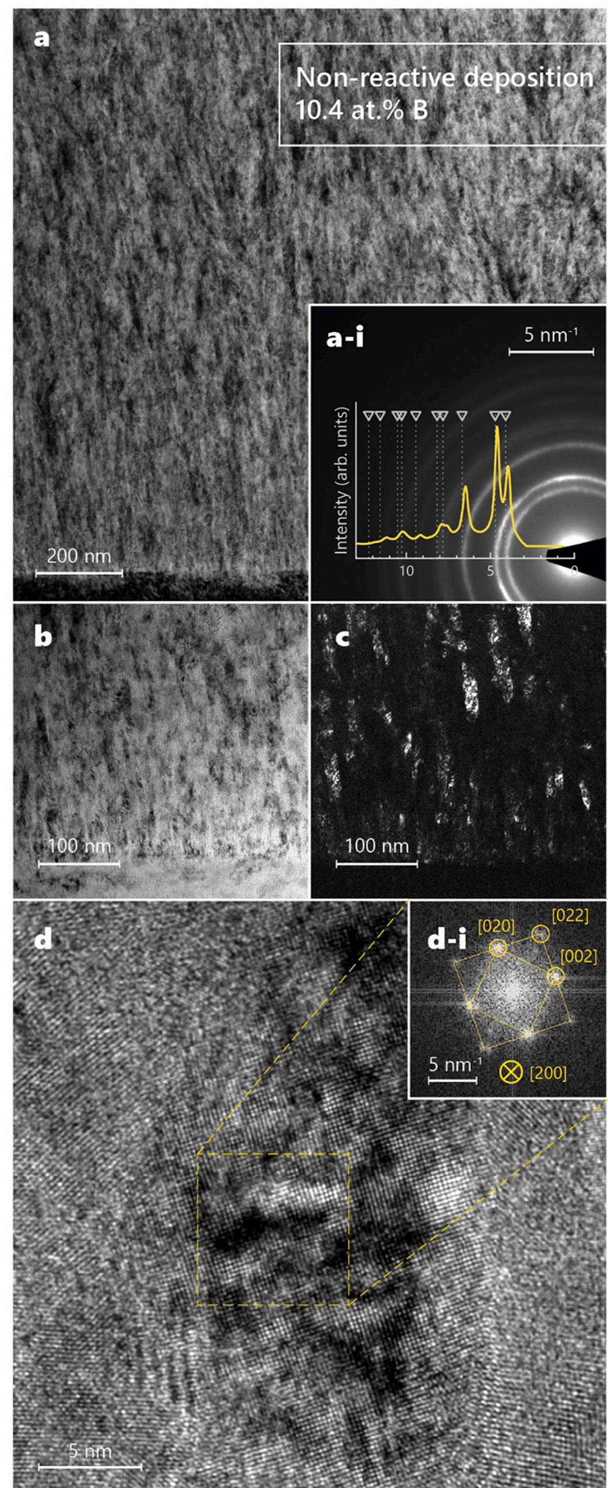

Fig. 6. TEM micrographs of the non-reactively deposited coating with 10.4 at.% B. 6a shows an overview image of our coating including a SAED pattern with an overlay of the integrated intensity (CrystBox [56,57]), the triangles mark the TiN reference (00-038-1420). 6b shows a higher magnified image, 6c a dark field (111 and 200) image of the same area. 6d shows an HR image of several grains including inset d-i showing an FFT of the marked area (dashed square) including necessary information on the crystallographic orientation of the grain and the calculated reflections.

(111) XRD peak shifts to the left and the (200) peak shifts to the right. This indicated the formation of new phases, possibly TiB_2, whose (100) and (101) XRD peaks would be to the left respectively right side of the TiN peaks. The sharp peak at around 62° visible in some patterns originates from the Si (100) substrate (Cu-K_β reflection of the 400-lattice planes of Si), along with the 2Theta reflection at 33 and 56° (Cu-K_β reflection of the 200- and 311-lattice planes of Si). At the highest B content of 17.5 at.% (in the reactive case) all XRD peaks are already extremely broad.

The XRD patterns of the non-relatively sputtered Ti-B-N coatings using a TiN and a TiB_2 target, respectively, (see Fig. 4b) show increasing broadening as well as shift (to smaller diffraction angles) of the TiN related peaks with increasing B content. The shift in XRD peak positions suggests a nearly linear lattice parameter increase from about 4.25 ± 0.001 Å to 4.29 ± 0.001 Å with increasing B content from 0 to 10.4 at.% B – being the maximum for these co-sputtered films. The ab initio obtained lattice parameter is 4.53 Å for fcc-TiB and 4.31 Å for fcc-$TiN_{0.75}B_{0.25}$, where B would fully substitute 25 at.% N of an fcc-$TiN_{1-x}B_x$ lattice (x = 0.25 equal to an overall B content of 12.5 at.%) [10]. Chemically, the non-reactively sputtered Ti-B-N coatings are along the quasi-binary TiN-TiB_2 tie-line, and if B would also substitute for Ti (to allow a chemistry along this tie-line) the ab initio obtained lattice parameter is 4.27 Å for fcc-$Ti_{0.875}B_{0.125}N_{0.75}B_{0.25}$ (overall B content of 18.75 at.%). Thus, our experimentally obtained lattice parameters are between these ab-initio calculated values, suggesting that B mainly substitutes for N but also partly for Ti in an fcc-TiN based lattice. This agrees with the XPS measurements suggesting Ti-B, B—N, and TiB_2 bonds. The coating with the highest B content of 23.9 at.% was prepared non- reactively from the $(TiN)_{0.5}(TiB_2)_{0.5}$ compound target. There, the XRD peaks are extremely broad with low intensity and positions between the TiN and TiB_2 standard values. Actually, this pattern is very similar to those obtained from Ti-B-N coatings, which are prepared by non-reactive sputtering of one segmented TiN-TiB_2 target (half TiN and half TiB_2) [52]. Detailed TEM studies showed that these coatings are composed of TiN and TiB_2 nm-sized crystals embedded in amorphous boundary layers [25].

TEM investigations of our coatings – exemplarily shown here for a reactively sputtered film with 9 at.% boron (see Fig. 5) as well as for a non-reactively grown film with 10.5 at.% boron (see Fig. 6) – clearly show their compact, dense growth morphology. The overview (in bright field mode) of the entire cross-section, Fig. 5a, shows such a fine-fibrous growth morphology for the reactively prepared film. The inset (a-i) is a quarter SAED pattern (obtained with a 750 nm diameter aperture positioned in the middle of the coating's cross section) including the integrated intensity of the full ring pattern with the relevant TiN reference positions (indicated with triangle symbols). These clearly show a fully cubic structure without any sign of other crystalline phases. Fig. 5b is a detailed bright field micrograph in the vicinity of the interface to the Si-substrate, and Fig. 5c is the same area in dark field mode for which we used the (111) and (200) reflections to contrast single grains. The latter is used to quantitatively evaluate the column width, which is 6.6 ± 1.2 nm. The HRTEM image (see Fig. 5d) of a surface-near-region of our coating shows more crystallites with different orientations, but all with an fcc-TiN based structure (see the FFT given in inset d-i). The dashed quarter-circles in this inset mark the TiN reference rings for the 111, 200, and 220 orientation. The dashed small circles mark the selected regions for the inverse FFT shown in inset d-ii, indicating a similar grain size as obtained from the lower magnification DF images (see Fig. 5c). The cross sectional HR-TEM studies of this reactively sputtered film with 9 at.% B do not show clear signs of amorphous grain and column boundary phases. Considering that the reactively sputtered Ti-B-N films: (*i*) are chemically almost perfectly positioned along the quasi-binary TiN-BN tie-line, (*ii*) have dominating BN bonds next to Ti—B, (*iii*) and have only one crystalline phase based on TiN with essentially no lattice parameter variation at least up to 9 at.% B, these HR-TEM studies suggest that B substitutes the metal species of an fcc-TiN based crystal. Our

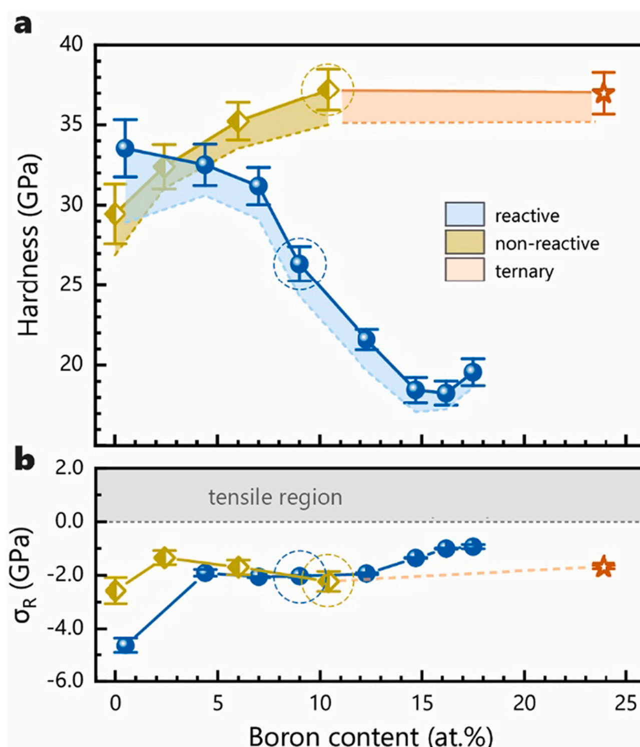

Fig. 7. Hardness and residual stress of out Ti-B-N coatings. panel a shows the hardness of our coatings with respect to the Boron content. The symbols and lines thereby represent the measured hardness values, whereas the shadowed region underneath represent the measured hardness corrected for the residual stress. Panel b shows the residual stress values.

conclusion is also manifested by the detailed XPS studies of reactively sputtered Ti-B-N coatings having different B content (with chemistries also along the TiN-BN tie line). There, with increasing B content the B—N bonds increase in intensity as well as the TiB_2 bonds, but the TiB_2 bonds show highest intensity for medium B contents.

The non-reactively prepared Ti-B-N coating, with a similar B content of 10.4 at.%, shows a very similar growth morphology with probably slightly larger grains, see the TEM overview image in Fig. 6a. The inset (a-i) is a SAED taken from the midfield of the coating's cross section. Again, the integrated pattern shows no other crystalline phase than cubic TiN (referenced with triangles). A higher magnification of the substrate near region is shown in Fig. 6b. The corresponding dark field image selecting the (111) and (200) reflections of c-TiN (Fig. 6c) allowed evaluating the average column width to be 16.3 ± 1.8 nm. Thus, significantly larger as the 6.6 ± 1.2 nm obtained for the reactively sputtered coating (with a similar B content of 9 at.%) and in agreement with the overall impression, compare Figs. 5a and 6a. HRTEM investigations (Fig. 6c) also show for this coating no indication for an excessive amorphous-like boundary phase and the column width of about 15.5 nm (from this surface near region) very well agrees with the column widths obtained from the dark field image, see Fig. 6c. The inset d-I shows an FFT of the selected region (marked with yellow dashed lines). This particular grain is imaged in [200] direction, hence the spots in the FFT are assigned to the ⟨200⟩ and ⟨220⟩ families, respectively. Considering that chemically the non-reactively sputtered Ti-B-N coatings are along the quasi-binary TiN-TiB_2 tie line, and that the only crystalline phase present (up to a B content of 10.4 at.%) is fcc-TiN-based (with increasing lattice parameter for increasing B content), the TEM studies suggest that B substitutes most probably for Ti and N in this crystal structure. Only if B also substitutes for N, the lattice parameter of the fcc-TiN based crystals increases with increasing B content. The substation of N with B also allows for the dominating Ti—B bonds

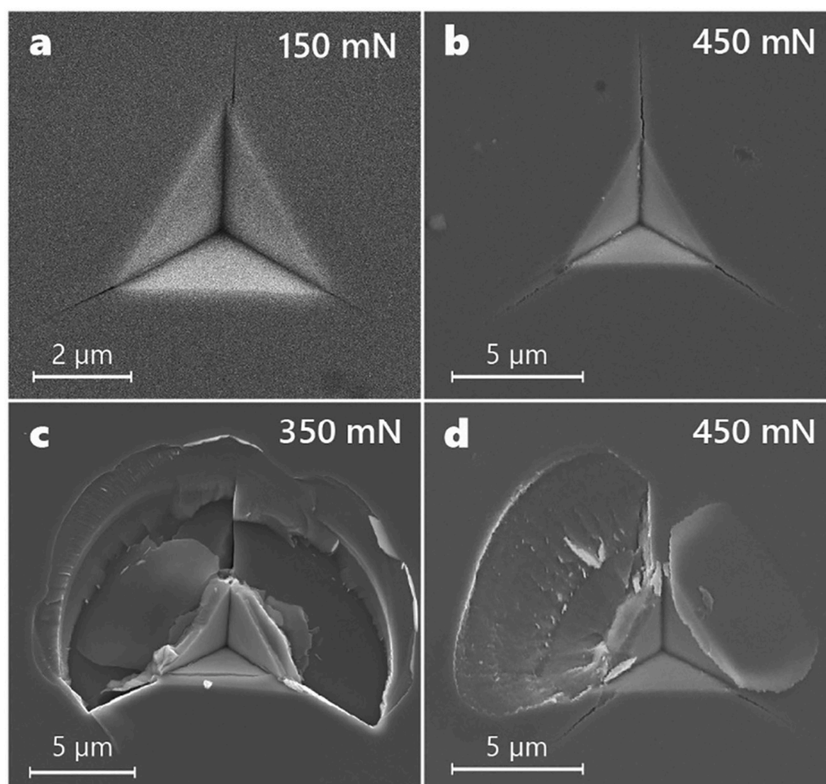

Fig. 8. Residual imprints of our cube corner indentation experiments. Panels a and c show the residual imprint of a reactively deposited coating with 9.0 at.% B, and panels b and d show similar behavior for a non-reactively deposited coating (6.0 at.%). The maximum indentation forces were 150 mN, 450 mN, 350 mN, and 450 mN for a, b, c, and d respectively.

obtained by XPS of the 10.4 at.% B containing coating. The occurrence of only this phase also partly explains the larger column width compared to the reactive case, where a competing second phase is present.

Although for the reactively as well as non-reactively sputtered Ti-B-N coatings up to about 10 at.% B no major contribution of an amorphous boundary phase was found during the TEM studies, and the only crystalline phase is an fcc-TiN based structure, this structure provides different bond contributions from both series. For the reactively sputtered films, B mainly substitutes for Ti, leading to BN bonds (but in an fcc-based lattice). In contrast, for the non-reactively sputtered films, B substitutes for Ti as well as for N, leading to additional Ti—B bonds (in an fcc-based lattice). This different bond situation leads to different mechanical properties (as proven by mechanical investigations, next paragraph).

3.3. *Mechanical properties*

Fig. 7a shows the hardness as a function of the Boron content. The data points and lines thereby show the measured data and the shadowing underneath the measured values show corrected values. The correction was made by considering the residual biaxial stress values obtained from the curvature of coated Si stripes (shown in Fig. 7b). This is justified since compressive residual stresses directly impede the penetration of the indenter, whereas tensile residual stresses support it. For simplicity and based on numerous investigations we used a 1-to-1 correlation (i.e., -1 GPa stresses increase the measured hardness value by 1 GPa, which is a rather conservative value - for comparison, Karlsson et al. found a correlation between ~1.3 to 1.9 for Ti(C,N) [53]). This correction hence allows analyzing the hardness without the influence of residual stresses. The latter shows a strong dependence on the B content for the reactively prepared coatings, decreasing from -4.6 ± 0.28 to -0.9 ± 0.08 GPa upon increasing the B content. Comparing the stresses with the XRD patterns (see Fig. 4) indicate, that the highest compressive stresses of -4.6 ± 0.28 GPa are obtained for the coating with a pronounced (200) oriented growth. From 4.4 to 9.0 at.% boron, where the structure is dominated by TiN based crystals with a preferred (111) growth orientation, the coatings show compressive residual stresses of ~ -2.0 GPa. Higher B contents promoting the formation of nanocrystals with random orientation, cause residual compressive stresses between -2.0 ± 0.04 to -0.9 ± 0.08 GPa. The non-reactively prepared coatings exhibit biaxial compressive residual stresses between -2.5 ± 0.48 GPa (0 at.% B) and -1.3 ± 0.25 GPa (2 at.% B). Although the structure changes from single-phase TiN-based to nanocomposite upon increasing the B content from 10.4 at.% to 23.9 at.%, the difference in compressive residual stresses is only 0.1 GPa – see the ternary line in Fig. 7a and b.

Both coating series start with a hardness of about 29 ± 1.9 to 33 ± 1.8 GPa, which increases to around 37 ± 1.3 GPa for the non-reactively prepared coatings with increasing B content to 10.4 at.% (remaining in the single-phase TiN-based structure) nearly following a square root of B content relationship (in agreement to Fleischer). Further increasing the B content to 23.9 at.%, which causes the formation of nanocrystalline TiN and TiB2 phases, does not influence the hardness anymore. The hardness of the reactively prepared coatings peaks already with 33 ± 1.8 GPa at the beginning, and then decreases to only 18 ± 0.7 GPa upon further increasing the B content to 14.7 at.%. The two coatings with even higher B contents (up to 17.5 at.%) show also only H values below 19.5 GPa. Comparing the reactively with the non-reactively prepared coating containing at about 10 at.% B, for which we have a detailed XPS (Fig. 3) and TEM study (Figs. 5 and 6), highlights the importance of the bond characteristics for the hardness. This non-reactively prepared coating, for which the Ti—B bonds dominate, obtains a hardness of about 37 ± 1.3 GPa being nearly 12 GPa higher compared to the reactively prepared one with dominating B—N bonds. Their structure is

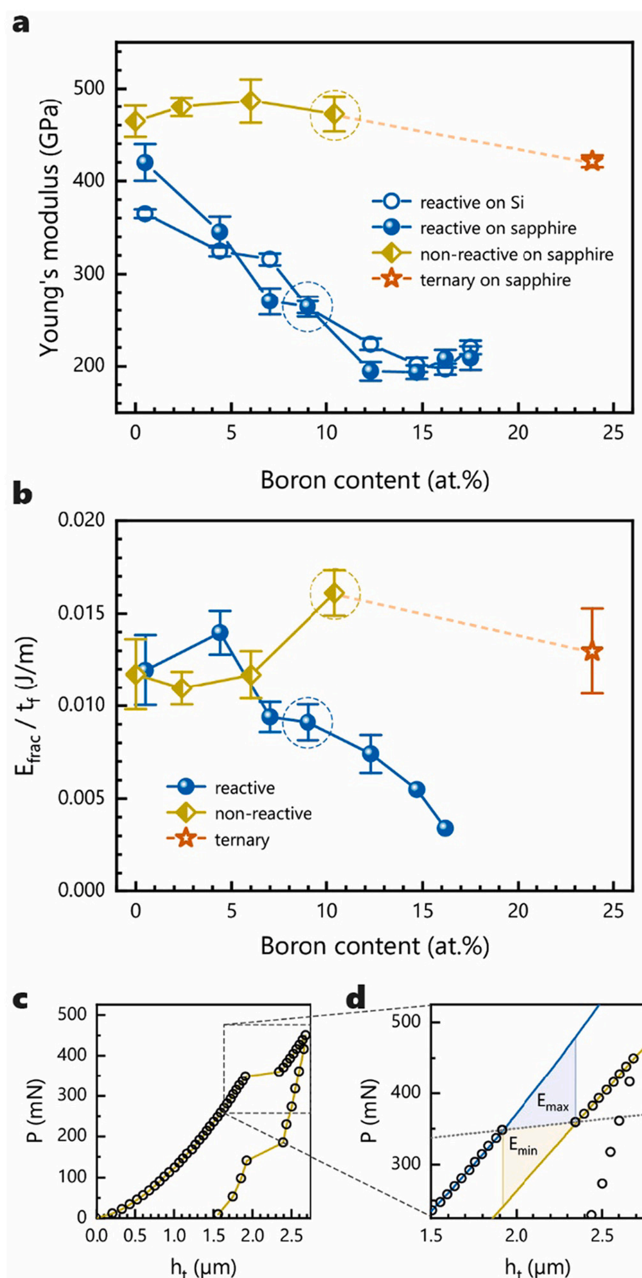

Fig. 9. Young's modulus of our thin films with respect to the Boron content (9a). 9b shows the energy necessary to cause fracture through the whole film thickness during cube-corner indentation experiments. 9c shows an exemplary force-displacement curve of such an indentation, and 9d shows a detail of the pop-in event and highlights the areas which represent E_{min} and E_{max}. The solid-blue, solid-yellow, and dotted-grey lines are fitted data before, after, and during the crack event respectively.

comparable with single-phase based TiN – the compressive residual stresses are identical with about 2 GPa – and also the growth morphology itself is not significantly different. The minor differences in crystal structure and growth morphology would not result in a 12 GPa hardness difference.

The obtained indentation modulus of our reactively prepared coatings (see Fig. 9a) shows a strong dependence on the B content similar to their hardness, decreasing from 420 ± 20 to 193 ± 7 GPa (measured on sapphire) upon increasing the B content to 14.7 at.%. The non-reactively prepared ones exhibit an increase in E from 464 ± 17 to 486 ± 24 GPa upon increasing B to 6.7 at.%, but a further increase in B to 23.9 at.% leads to a reduction in E to 421 ± 6 GPa. Especially this coating, non-reactively prepared from the $(TiN)_{0.5}(TiB_2)_{0.5}$ compound target should be capable of a high resistance against fracture. This estimation substantiates on the combination of a dense nanocrystalline growth morphology with a high hardness and highest H^3/E^2 ratio of 0.248 GPa among the coatings studied here. The latter allows estimating the ability for energy-dissipation at plastic deformation during loading [54].

Experimental verification of the fracture resistance is obtained by 150, 350, and 450 mN loaded cube corner indentations of the coatings grown on sapphire. Exemplarily, four characteristic residual imprints after these experiments are presented in Fig. 8, showing the two major different types of crack-growths observed. Either the cracks form at the corners and tear away from the center of the indent (Fig. 8a and b) or circular cracks form and corresponding chipping occurs (see Fig. 8c and d). Although there are methods to evaluate the fracture toughness for both types of crack formation [55], a direct comparison would lead to misinterpretations. Therefore, we minimized this possible error by evaluating the fracture energy, E_{frac}, normalized to the film thickness, t_f. Fig. 9b shows this normalized fracture energy as a function of the B content of the reactively and non-reactively sputtered Ti-B-N coatings. The energy was obtained from the area under the load-deflection curve, which was recorded during the indentation process. For each case, the minimum and maximum energy were averaged for the calculation. The minimum energy is obtained by using the fitted curve after the pop-in event and the maximum energy is obtained by using the fit before the pop-in event (see Fig. 9d).

The normalized fracture energy peaks with 0.014 ± 0.001 J/m at a B content of 4.5 at.% for the reactively sputtered coatings. A further increase in B causes the E_{frac}/t_f to decrease to values below 0.010 J/m and even 0.005 J/m for the highest B content of 15.7 at.%. The non-reactively prepared coatings always showed values above 0.010 J/m, with a peak of 0.016 ± 0.001 J/m for 10.4 at.% B. Again, if we compare the coatings with about 10 at.% B, clearly the non-reactively prepared Ti-B-N outperforms the reactively prepared one. The observed progressions with the B content suggest that this is certainly not the dominating factor influencing the fracture energy. Hence, we propose that, again, the binding of boron is the critical factor determining the fracture properties of our thin films. This assumption is substantiated with the measured higher Young's modulus: In the absence of plastic deformation, a higher modulus goes along with higher toughness values. Nevertheless, to gain intrinsic fracture toughness values K_{IC}, which are quantitatively comparable with other studies, microcantilever bending tests would be suggested.

4. Summary and conclusion

We have successfully deposited Ti-B-N coatings using two different magnetron sputtering deposition routes: (*i*) Ti and TiB_2 targets in reactive, nitrogen-containing atmosphere, as well as (*ii*) TiN and TiB_2 or a Ti-B-N target in a non-reactive atmosphere (pure Ar). These deposition routes lead to significant differences in their chemical composition. The reactive films are located along the TiN-BN tie line in a ternary phase diagram, while the non-reactive depositions are located along the TiN-TiB_2 tie line. This is also reflected in the detailed XPS spectra, indicating an increased amount of B—N bonds in reactively deposited coatings compared to increased amounts of Ti-B bonds for non-reactively deposited films. In addition, mass spectroscopy analysis shows, that the fraction $N^+/(N^+ + N_2^+)$ is 51% during non-reactive discharges and only 15% during reactive discharges. Hence, there is especially an oversupply of the less-reactive N_2^+ ions with respect to Ti ions during reactive sputtering next to excess N_2. As a further consequence, fewer N^+ ions are highly effective during non-reactively sputter deposition leading to a higher deposition rate for the non-reactive case, whereas excess N_2 decorating the growing film in the reactive case, and hence slowing it down. For both deposition routes, fcc dominated structures are observed, whereas as only at high boron contents difference appear –

above 14.7 at.% B in the reactive case and at 23.9 at.% B in the non-reactive case extreme peak broadening due to small crystallites embedded in an amorphous grain boundary matrix.

However, no strong morphological variations are visible during TEM analysis, but a clear difference in column width of 6.6 ± 1.2 nm for the reactive case compared to 16.3 ± 1.8 nm for its non-reactively counterpart at around 10 at.% B can be seen. This is a strong indication, that for the reactively sputtered films, B mainly substitutes for Ti, leading to B—N bonds (but in an fcc-based lattice), whereas for the non-reactively sputtered films, B substitutes for Ti as well as for N, leading to additional Ti—B bonds (in an fcc-based lattice).

This difference in bonding characteristics also strongly contributes to the mechanical properties. We measure similar hardness, modulus of elasticity, and fracture energy values for TiN, or small Boron contents, but with increasing amounts of Boron the fracture behavior at the highest hardness differs significantly. At around 10 at.% Boron, we observe hardness and indentation modulus values of 35 ± 1.7 and 472 ± 19 GPa for the non-reactively deposited coating, compared to 25 ± 1.1 and 264 ± 11 GPa for the reactively one. Furthermore, improved fracture properties at higher hardness, are indicated by increased fracture energies during cube corner indentations – 0.016 ± 0.0012 J/m compared to 0.009 ± 0.0010 J/m for the non-reactive versus the reactive state at around 10 at.% B, respectively. This trend is even more pronounced at very high Boron contents.

In summary, non-reactive deposition offers a straightforward way to dissolve Boron in fcc structure TiN, resulting in increased mechanical properties, especially hardness but also fracture tolerance at high Boron contents.

CRediT authorship contribution statement

R. Hahn: Conceptualization, Investigation, Writing – original draft, Visualization, Software. **A. Tymoszuk:** Investigation, Formal analysis. **T. Wojcik:** Investigation, Formal analysis. **A. Kirnbauer:** Investigation, Formal analysis. **T. Kozák:** Investigation, Writing – review & editing, Resources. **J. Capek:** Investigation, Resources. **M. Sauer:** Investigation, Formal analysis, Writing – review & editing. **A. Foelske:** Writing – review & editing, Resources. **O. Hunold:** Writing – review & editing, Funding acquisition. **P. Polcik:** Writing – review & editing, Funding acquisition, Resources. **P.H. Mayrhofer:** Writing – review & editing, Conceptualization, Project administration. **H. Riedl:** Supervision, Conceptualization, Writing – review & editing, Project administration, Funding acquisition.

Declaration of competing interest

The authors declare that they have no known competing financial interests or personal relationships that could have appeared to influence the work reported in this paper.

Acknowledgment

The financial support by the Austrian Federal Ministry for Digital and Economic Affairs, the National Foundation for Research, Technology and Development and the Christian Doppler Research Association is gratefully acknowledged (Christian Doppler Laboratory "Surface Engineering of high-performance Components"). We also thank for the financial support of Plansee SE, Plansee Composite Materials GmbH, and Oerlikon Surface Solutions AG. In addition, we want to thank the X-ray center (XRC, AIC) of TU Wien for beam time, as well as the electron microscopy center - USTEM TU Wien - for using the SEM and TEM facilities.

References

[1] I. Petrov, L. Hultman, U. Helmersson, J.-E. Sundgren, J.E. Greene, Microstructure modification of TiN by ion bombardment during reactive sputter deposition, Thin Solid Films 169 (1989) 299–314, https://doi.org/10.1016/0040-6090(89)90713-X.

[2] H. Ljungcrantz, L. Hultman, J.-E. Sundgren, L. Karlsson, Ion induced stress generation in arc-evaporated TiN films, J. Appl. Phys. 78 (1995) 832–837, https://doi.org/10.1063/1.360272.

[3] M. Lattemann, U. Helmersson, J.E. Greene, Fully dense, non-faceted 111-textured high power impulse magnetron sputtering TiN films grown in the absence of substrate heating and bias, Thin Solid Films 518 (2010) 5978–5980, https://doi.org/10.1016/j.tsf.2010.05.064.

[4] U. Helmersson, S. Todorova, S.A. Barnett, J.E. Sundgren, L.C. Markert, J.E. Greene, Growth of single-crystal TiN/VN strained-layer superlattices with extremely high mechanical hardness, J. Appl. Phys. 62 (1987) 481–484, https://doi.org/10.1063/1.339770.

[5] P.E. Hovsepian, D.B. Lewis, W.D. Münz, Recent progress in large scale manufacturing of multilayer/superlattice hard coatings, Surf. Coat. Technol. 133–134 (2000) 166–175, https://doi.org/10.1016/S0257-8972(00)00959-2.

[6] W. Münz, Titanium aluminum nitride films: a new alternative to TiN coatings, J. Vac. Sci. Technol. A Vac. Surf. Film 4 (1986) 2717–2725, https://doi.org/10.1116/1.573713.

[7] O. Knotek, M. Böhmer, T. Leyendecker, On structure and properties of sputtered Ti and Al based hard compound films, J. Vac. Sci. Technol. A Vac. Surf. Film 4 (1986) 2695–2700, https://doi.org/10.1116/1.573708.

[8] S. Münsterer, K. Kohlhof, Cavitation protection by low temperature TiCN coatings, Surf. Coat. Technol. 74–75 (1995) 642–647, https://doi.org/10.1016/0257-8972(95)08265-4.

[9] J.M. Schneider, A. Voevodin, C. Rebholz, A. Matthews, J.H.C. Hogg, D.B. Lewis, M. Ives, X-ray diffraction investigations of magnetron sputtered TiCN coatings, Surf. Coat. Technol. 74–75 (1995) 312–319, https://doi.org/10.1016/0257-8972(95)08238-7.

[10] P.H. Mayrhofer, M. Stoiber, Thermal stability of superhard Ti–B–N coatings, Surf. Coat. Technol. 201 (2007) 6148–6153, https://doi.org/10.1016/j.surfcoat.2006.08.132.

[11] C. Fuger, V. Moraes, R. Hahn, H. Bolvardi, P. Polcik, H. Riedl, P.H. Mayrhofer, Influence of Tantalum on phase stability and mechanical properties of WB2, MRS Communications 9 (2019) 375–380, https://doi.org/10.1557/mrc.2019.5.

[12] Y.G. Shen, Y.H. Lu, Z.J. Liu, Microstructure evolution and grain growth of nanocomposite TiN-TiB2 films: experiment and simulation, Surf. Coat. Technol. 200 (2006) 6474–6478, https://doi.org/10.1016/j.surfcoat.2005.11.065.

[13] P. Losbichler, C. Mitterer, P.N. Gibson, W. Gissler, F. Hofer, P. Warbichler, Co-sputtered films within the quasi-binary system TiN-TiB2, Surf. Coat. Technol. 94–95 (1997) 297–302, https://doi.org/10.1016/S0257-8972(97)00440-4.

[14] C. Mitterer, P. Losbichler, F. Hofer, P. Warbichler, P. Gibson, W. Gissler, Nanocrystalline hard coatings within the quasi-binary system TiN–TiB2, Vacuum. 50 (1998) 313–318, https://doi.org/10.1016/S0042-207X(98)00059-1.

[15] O. Knotek, F. Jungblut, R. Breidenbach, Magnetron-sputtered superhard coatings within the system TiBCN, Vacuum. 41 (1990) 2184–2186, https://doi.org/10.1016/0042-207X(90)94220-K.

[16] J. Xu, Z. Li, Z.H. Xie, P. Munroe, Uniting superhardness and damage-tolerance in a nanosandwich-structured Ti-B-N coating, Scr, Mater. 74 (2014) 88–91, https://doi.org/10.1016/j.scriptamat.2013.11.004.

[17] C. Mitterer, P.H. Mayrhofer, M. Beschliesser, P. Losbichler, P. Warbichler, F. Hofer, P.N. Gibson, W. Gissler, H. Hruby, J. Musil, J. Vlček, Microstructure and properties of nanocomposite Ti–B–N and Ti–B–C coatings, Surf. Coat. Technol. 120–121 (1999) 405–411, https://doi.org/10.1016/S0257-8972(99)00489-2.

[18] D.V. Shtansky, F.V. Kiryukhantsev-Korneev, A.N. Sheveiko, I.A. Bashkova, O. V. Malochkin, E.A. Levashov, N.B. D'yakonova, I.V. Lyasotsky, Structure and properties of Ti-B-N, Ti-Cr-B-(N), and Cr-B-(N) coatings deposited by magnetron sputtering of targets prepared by self-propagating high-temperature synthesis, Phys. Solid State 47 (2005) 252–262, https://doi.org/10.1134/1.1866403.

[19] R.A. Andrievski, G.V. Kalinnikov, Physical-mechanical and physical-chemical properties of thin nonostructured boride/nitride films, Surf. Coat. Technol. 142–144 (2001) 573–578, https://doi.org/10.1016/S0257-8972(01)01246-4.

[20] M. Tamura, H. Kubo, Ti-B-N coatings deposited by magnetron arc evaporation, Surf. Coat. Technol. 54–55 (1992) 255–260, https://doi.org/10.1016/S0257-8972(09)90059-7.

[21] R. Wiedemann, V. Weihnacht, H. Oettel, Structure and mechanical properties of amorphous Ti–B–N coatings, Surf. Coat. Technol. 116–119 (1999) 302–309, https://doi.org/10.1016/S0257-8972(99)00130-9.

[22] P. Holubář, M. Jılek, M. Šıma, Nanocomposite nc-TiAlSiN and nc-TiN–BN coatings: their applications on substrates made of cemented carbide and results of cutting tests, Surf. Coat. Technol. 120–121 (1999) 184–188, https://doi.org/10.1016/S0257-8972(99)00483-1.

[23] C. Mitterer, M. Rauter, P. Rödhammer, Sputter deposition of ultrahard coatings within the system Ti-B-C-N, Surf. Coat. Technol. 41 (1990) 351–363, https://doi.org/10.1016/0257-8972(90)90146-4.

[24] P. Karvankova, M.G.J. Veprek-Heijman, O. Zindulka, A. Bergmaier, S. Veprek, Superhard nc-TiN/a-BN and nc-TiN/a-TiBx/a-BN coatings prepared by plasma CVD and PVD: a comparative study of their properties, Surf. Coat. Technol. 163–164 (2003) 149–156, https://doi.org/10.1016/S0257-8972(02)00492-9.

[25] P.H. Mayrhofer, C. Mitterer, J.G. Wen, I. Petrov, J.E. Greene, Thermally induced self-hardening of nanocrystalline Ti–B–N thin films, J. Appl. Phys. 100 (2006), 044301, https://doi.org/10.1063/1.2222406.

[26] P.H. Mayrhofer, M. Stoiber, C. Mitterer, Age hardening of PACVD TiBN thin films, Scr, Mater. 53 (2005) 241–245, https://doi.org/10.1016/j.scriptamat.2005.03.031.

[27] T.P. Mollart, M. Baker, J. Haupt, A. Steiner, P. Hammer, W. Gissler, Nanostructured titanium boron nitride coatings of very high hardness, Surf. Coat. Technol. 74–75 (1995) 491–496, https://doi.org/10.1016/0257-8972(95)08252-2.

[28] C. Héau, J. Terrat, Ultrahard Ti–B–N coatings obtained by reactive magnetron sputtering of a Ti–B target, Surf. Coat. Technol. 108–109 (1998) 332–339, https://doi.org/10.1016/S0257-8972(98)00621-5.

[29] J.C. Slater, Atomic radii in crystals, J. Chem. Phys. 41 (1964) 3199–3204, https://doi.org/10.1063/1.1725697.

[30] B. Cordero, V. Gómez, A.E. Platero-Prats, M. Revés, J. Echeverría, E. Cremades, F. Barragán, S. Alvarez, Covalent radii revisited, J. Chem. Soc. Dalton Trans. (2008) 2832–2838, https://doi.org/10.1039/b801115j.

[31] N.J. Petch, The cleavage strength of polycrystals, J. Iron Steel 174 (1953) 25–28. https://ci.nii.ac.jp/naid/10019881123/. (Accessed 4 June 2019).

[32] E.O. Hall, The deformation and ageing of mild steel: III discussion of results, Proc. Phys. Soc. Sect. B 64 (1951) 747–753, https://doi.org/10.1088/0370-1301/64/9/303.

[33] T. Glechner, S. Lang, R. Hahn, M. Alfreider, V. Moraes, D. Primetzhofer, J. Ramm, S. Kolozsvári, D. Kiener, H. Riedl, Correlation between fracture characteristics and valence electron concentration of sputtered Hf-C-N based thin films, Surf. Coat. Technol. 399 (2020), 126212, https://doi.org/10.1016/j.surfcoat.2020.126212.

[34] T. Glechner, R. Hahn, T. Wojcik, D. Holec, S. Kolozsvári, H. Zaid, S. Kodambaka, P. H. Mayrhofer, H. Riedl, Assessment of ductile character in superhard Ta-C-N thin films, Acta Mater. (2019), https://doi.org/10.1016/j.actamat.2019.08.015.

[35] P.H. Mayrhofer, C. Mitterer, L. Hultman, H. Clemens, Microstructural design of hard coatings, Prog, Mater. Sci. 51 (2006) 1032–1114, https://doi.org/10.1016/j.pmatsci.2006.02.002.

[36] J.H. Scofield, Hartree-Slater subshell photoionization cross-sections at 1254 and 1487 eV, J. Electron Spectrosc. Relat. Phenom. 8 (1976) 129–137, https://doi.org/10.1016/0368-2048(76)80015-1.

[37] W.C. Oliver, G.M. Pharr, An improved technique for determining hardness and elastic modulus using load and displacement sensing indentation experiments, J. Mater. Res. 7 (1992) 1564–1583, https://doi.org/10.1557/JMR.1992.1564.

[38] J. Menčík, D. Munz, E. Quandt, E.R. Weppelmann, M.V. Swain, Determination of elastic modulus of thin layers using nanoindentation, J. Mater. Res. 12 (1997) 2475–2484, https://doi.org/10.1557/jmr.1997.0327.

[39] X. Li, D. Diao, B. Bhushan, Fracture mechanisms of thin amorphous carbon films in nanoindentation, Acta Mater. 45 (1997) 4453–4461, https://doi.org/10.1016/S1359-6454(97)00143-2.

[40] K. Van Aeken, S. Mahieu, D. Depla, The metal flux from a rotating cylindrical magnetron: a Monte Carlo simulation, J. Phys. D. Appl. Phys. 41 (2008), https://doi.org/10.1088/0022-3727/41/20/205307.

[41] R. Ranjan, J.P. Allain, M.R. Hendricks, D.N. Ruzic, Absolute sputtering yield of Ti/TiN by Ar+/N+ at 400–700 eV, J. Vac. Sci. Technol. A Vac. Surf. Film 19 (2001) 1004–1007, https://doi.org/10.1116/1.1362678.

[42] M. Berger, M. Larsson, S. Hogmark, Evaluation of magnetron-sputtered TiB2 intended for tribological applications, Surf. Coat. Technol. 124 (2000) 253–261, https://doi.org/10.1016/S0257-8972(99)00638-6.

[43] P.H. Mayrhofer, C. Mitterer, J.G. Wen, J.E. Greene, I. Petrov, Self-organized nanocolumnar structure in superhard TiB2 thin films, Appl. Phys. Lett. (2005), https://doi.org/10.1063/1.1887824.

[44] B. Bakhit, I. Petrov, J.E. Greene, L. Hultman, J. Rosén, G. Greczynski, Controlling the B/Ti ratio of TiB x thin films grown by high-power impulse magnetron sputtering, J. Vac. Sci. Technol. A Vac. Surf. Film 36 (2018), 030604, https://doi.org/10.1116/1.5026445.

[45] S.M. Aouadi, F. Namavar, T.Z. Gorishnyy, S.L. Rohde, Characterization of TiBN films grown by ion beam assisted deposition, Surf. Coat. Technol. 160 (2002) 145–151, https://doi.org/10.1016/S0257-8972(02)00330-4.

[46] J. Neidhardt, Z. Czigány, B. Sartory, R. Tessadri, M. O'Sullivan, C. Mitterer, Nanocomposite Ti–B–N coatings synthesized by reactive arc evaporation, Acta Mater. 54 (2006) 4193–4200, https://doi.org/10.1016/j.actamat.2006.05.014.

[47] R. Ali, E. Alkhateeb, F. Kellner, S. Virtanen, N. Popovska-Leipertz, Chemical vapor deposition of titanium based ceramic coatings on low carbon steel: characterization and electrochemical evaluation, Surf. Coat. Technol. 205 (2011) 5454–5463, https://doi.org/10.1016/j.surfcoat.2011.06.014.

[48] I. Dreiling, C. Raisch, J. Glaser, D. Stiens, T. Chassé, Characterization and oxidation behavior of MTCVD Ti-B-N coatings, Surf. Coat. Technol. 206 (2011) 479–486, https://doi.org/10.1016/j.surfcoat.2011.07.067.

[49] C.D. Wagner, A.V. Naumkin, A. Kraut-Vass, J.W. Allison, C.J. Powell, J. R. Rumble Jr., NIST standard reference database 20, version 3.4 (web version), in: Natl. Inst. Stand. Technol. Gaithersburg, MD. 20899, 2003.

[50] J. Stuart, A. Hohenadel, X. Li, H. Xiao, J. Parkey, C.P. Rhodes, S. Licht, The net discharge mechanism of the VB 2/air battery, J. Electrochem. Soc. 162 (2015) A192–A197, https://doi.org/10.1149/2.0801501jes.

[51] E.O. Filatova, A.S. Konashuk, S.S. Sakhonenkov, A.A. Sokolov, V.V. Afanas'ev, Re-distribution of oxygen at the interface between γ-Al2O3 and TiN, Sci, Rep. 7 (2017) 1–14, https://doi.org/10.1038/s41598-017-04804-4.

[52] P.H. Mayrhofer, H. Willmann, C. Mitterer, Recrystallization and grain growth of nanocomposite Ti–B–N coatings, Thin Solid Films 440 (2003) 174–179, https://doi.org/10.1016/S0040-6090(03)00858-7.

[53] L. Karlsson, L. Hultman, J.E. Sundgren, Influence of residual stresses on the mechanical properties of TiCxN1-x (x = 0, 0.15, 0.45) thin films deposited by arc evaporation, Thin Solid Films 371 (2000) 167–177, https://doi.org/10.1016/S0040-6090(00)00996-2.

[54] T.Y. Tsui, G.M. Pharr, W.C. Oliver, C.S. Bhatia, R.L. White, S. Anders, A. Anders, I. G. Brown, Nanoindentation and nanoscratching of hard carbon coatings for magnetic disks, MRS Proc. 383 (1995) 447, https://doi.org/10.1557/PROC-383-447.

[55] S. Zhang, X. Zhang, Toughness evaluation of hard coatings and thin films, Thin Solid Films 520 (2012) 2375–2389, https://doi.org/10.1016/J.TSF.2011.09.036.

[56] M. Klinger, A. Jäger, Crystallographic tool box (CrysTBox): automated tools for transmission electron microscopists and crystallographers, J. Appl. Crystallogr. 48 (2015), https://doi.org/10.1107/S1600576715017252.

[57] M. Klinger, More features, more tools, more CrysTBox, J. Appl. Crystallogr. 50 (2017), https://doi.org/10.1107/S1600576717006793.